

Addition of Pore-Forming Agents and Their Effect on the Pore Architecture and Catalytic Behavior of Shaped Zeolite-Based Catalyst Bodies

Nikolaos Nikolopoulos, Luke A. Parker, Abhijit Wickramasinghe, Oscar van Veenhuizen, Gareth Whiting,* and Bert M. Weckhuysen*

Cite This: *Chem. Biomed. Imaging* 2023, 1, 40–48

Read Online

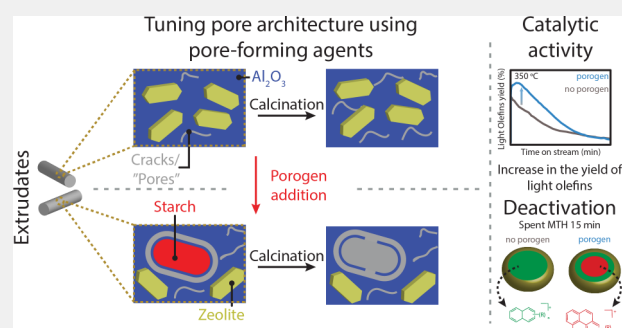
ACCESS |

Metrics & More

Article Recommendations

ABSTRACT: Porous materials, such as solid catalysts, are used in various chemical reactions in industry to produce chemicals, materials, and fuels. Understanding the interplay between pore architecture and catalytic behavior is of great importance for synthesizing a better industrial-grade catalyst material. In this study, we have investigated the modification of the pore architecture of zeolite-based alumina-bound shaped catalyst bodies via the addition of different starches as pore-forming agents. A combination of microscopy techniques allowed us to visualize the morphological changes induced and make a link between pore architecture, molecular transport, and catalytic performance. As for the catalytic performance in the methanol-to-hydrocarbons (MTH) reaction, pore-forming agents resulted in up to ~12% higher conversion, an increase of 74% and 77% in yield (14% and 13% compared to 8.6% and 7.7% of the reference sample in absolute yields) toward ethylene and propylene, respectively, and an improved lifetime of the catalyst materials.

KEYWORDS: Shaped catalyst bodies, Porogens, Methanol-to-hydrocarbons, Pore architecture, Coke formation, Molecular transport, Visualization



INTRODUCTION

Zeolite-based catalyst materials play a vital role in the production of essential chemicals, fuels, and materials.^{1–5} They are used in numerous fundamental catalytic processes, e.g., alkylation, isomerization, and cracking, due to their exceptional physicochemical properties, such as high porosity and tunable acidity.^{6–11} Commonly, the focus is on zeolite powders to gain more insight regarding their catalytic performance. However, to be used as a solid catalyst material in large-scale chemical production processes, shaped zeolite-based catalyst bodies with high catalytic performance have to be designed.^{5,12–14} Scaling up the production of a catalyst material is usually very challenging. Factors, such as the formulation and the shaping parameters, need to be considered as they can highly influence the overall properties of the final catalyst material.

The catalyst extrusion process is remarkably vaguely described in the open literature although practiced on a large scale in many manufacturing units all over the world. A significant number of components are usually required to formulate zeolite-containing shaped catalyst bodies, such as the active phase (zeolite), binder, peptizer, plasticizer, lubricant,

and porogen. Every component has a specific role related to the extrusion process and the final properties of the technical catalyst body. Firstly, the zeolite acts as the main active component, while the binder materials offer the mechanical strength needed to tolerate the harsh chemical reactor conditions. One or more inorganic material(s), such as alumina, silica, clays, zirconia, and titania, are usually chosen as binders. Acetic, citric, and nitric acid, among other acids, are used as peptizers to increase the homogeneity and dispersion of the binder particles. Finally, plasticizers and lubricants, e.g., methylcellulose and polyethylene glycol, reduce the viscosity and friction of the catalyst precursor paste material during the extrusion process.

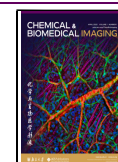
Pore-forming (or generating) agents, often called porogens, increase interparticle porosity in shaped catalyst bodies.

Received: December 30, 2022

Revised: February 4, 2023

Accepted: February 8, 2023

Published: March 6, 2023



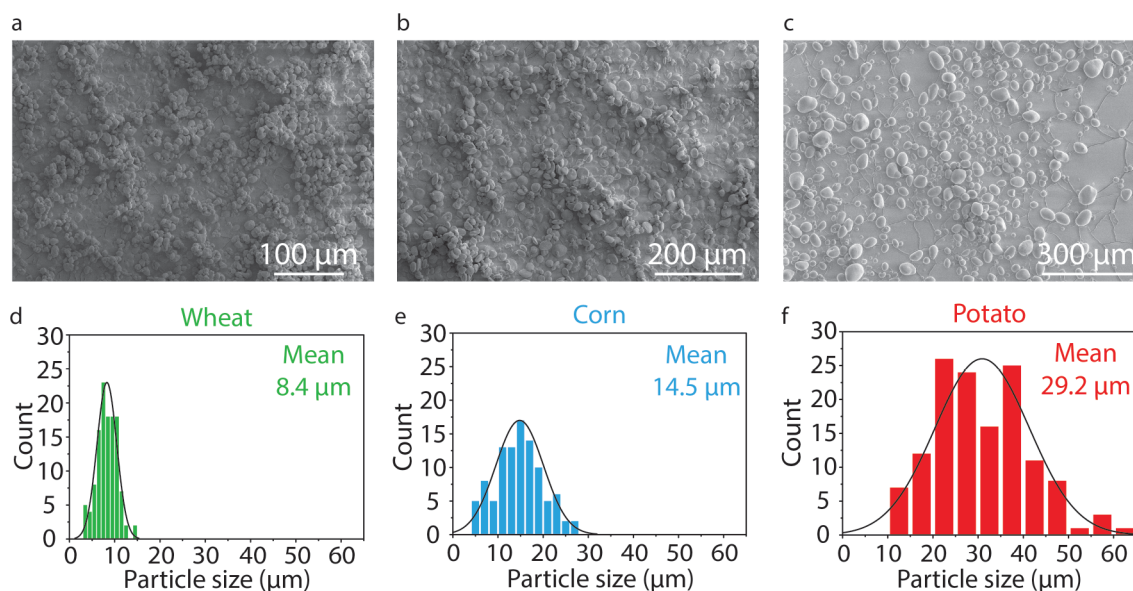


Figure 1. Morphological properties of the pore-forming agents. (a–c) SEM images of the wheat, rice, and potato starch, respectively, and (d–f) corresponding particle size distribution measured from the SEM images.

Starches, carbon black, sawdust, and flax have all been used to serve this purpose.^{14,15} Lubricants and plasticizers have a double role as they also act as pore-forming agents, resulting in a variety of meso- and macropores after their removal upon calcination.¹⁶ However, the effect of this type of additive in the pore architecture of shaped catalyst bodies has not yet been well understood due to a lack of the required visualization techniques.

A recent study of our research group underlines the importance of diffusion, accessibility, and catalytic performance using a simple way to visualize pore architecture and deactivation of zeolite-based shaped catalyst bodies.¹⁷ This study showed a strong correlation between pore architecture and catalytic performance in the methanol-to-hydrocarbons (MTH) reaction, among other important physicochemical observations. Chemical maps of the species formed within the zeolite-based catalyst extrudates showed a striking correlation between the location and type of the different hydrocarbon species formed. It was demonstrated that pore narrowing and the subsequent decrease in accessibility resulted in the entrapment of large aromatic molecules in the center of the catalyst body, which further oligomerize to form larger aromatic moieties. Overall, unlocking the interplay between pore structure, accessibility, and molecules formed during the reaction is the key for understanding catalytic performance in the MTH reaction and hopefully to design more active, selective, and stable catalyst materials.

In this study, we investigate the effect of the addition of pore-generating agents on the physicochemical properties and catalytic performance of industrial-grade zeolite-containing catalyst bodies. Three different starches derived from wheat, corn, and potato were used as pore-forming agents in zeolite-based alumina-bound catalyst extrudates. Focused ion beam-scanning electron microscopy (FIB-SEM) enabled us to visualize the modifications, induced by the addition of the porogens, on the morphology of the catalyst extrudates, while ammonia temperature-programmed desorption (NH₃-TPD) measurements showed an increase in the overall acidity of the materials under study. Interestingly, using starches in this

catalytic system also improved the catalytic activity. They increased not only the catalytic conversion but also the selectivity toward light olefins and led to a prolonged catalyst's lifetime. Diffusion studies and analysis of the spent samples using confocal fluorescence microscopy (CFM) in a time-resolved manner during the MTH reaction allowed us to establish a link between molecular transport, accessibility, acidity, and catalyst deactivation.

EXPERIMENTAL SECTION

Chemicals and Materials

The following chemicals, gases, and materials were used: pyridine (C₅H₅N, Merck, EMSURE), methanol (Acros, HPLC grade, 99.99% pure), N₂ (Linde, 99.998%), He (Linde, >99%), Ar (Linde, 99.998%), methylcellulose (Sigma-Aldrich, 4000 CP), acetic acid (Sigma-Aldrich, 99.5%), boehmite (CATAPAL D, SASOL), zeolite HZSM-5 (ACS material, MR 38), *N,N'*-bis(2,6-dimethyl phenyl)-perylene-3,4,9,10-tetracarboxylic diimide (PDI, Sigma-Aldrich), 20/45/100 nm probes (FluoSpheres, carboxylate-modified microspheres in Milli-Q water, ThermoFisher Scientific), and 7-hydroxy-3*H*-phenoxazin-3-one (resorufin, Sigma-Aldrich).

Preparation of Shaped Catalyst Bodies

Powder H-ZSM-5, boehmite (with a 50-50 wt % zeolite-to-boehmite ratio), and methylcellulose (2 wt % of the total amount of zeolite and binder) were mixed to acquire a homogeneous solid mixture, and acetic acid diluted in ultrapure water was added to form a paste. The formed paste was extruded in a Mini-Screw Extruder (Caleva) through a 2 mm diameter die plate of cylindrical shape. The catalyst extrudates were left to dry overnight and were then calcined in a fixed-bed reactor for 6 h at 300 °C (with a heating ramp of 10 °C/min) and then for 12 h at 600 °C/min under oxygen flow (120 mL/min). The sample described above is termed the reference sample.

In the case of the porogen samples, 30 wt % of the desired final product of wheat, corn, or potato starch was added in the first step together with the other solid materials to make the catalyst bodies. The rest of the procedure was followed as previously described.

Materials Characterization

X-ray diffraction (XRD) was measured on a Bruker D2 X-ray powder diffractometer with a Co K α X-ray tube ($\lambda = 1.7902 \text{ \AA}$) as the source. NH₃-TPD was measured on a Micromeritics AutoChemII 2920. FIB-SEM images were collected on a FEI Helios NanoLab G3 UC

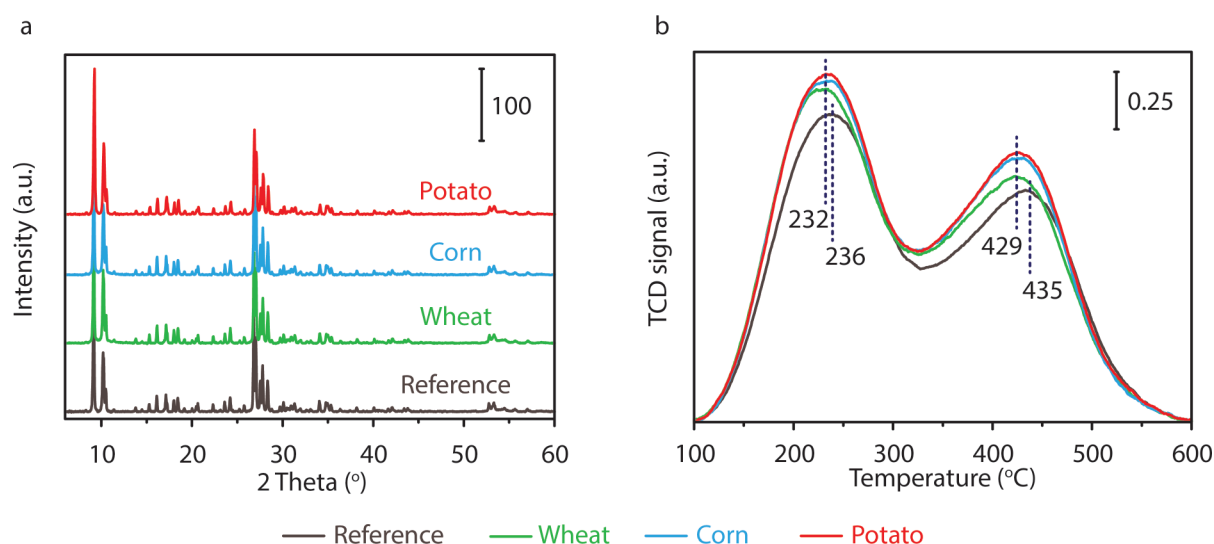


Figure 2. Structural and acidic properties upon addition of pore-forming agents. (a) XRD patterns. (b) NH_3 -TPD measurements for the reference sample and the wheat (green), corn (blue), and potato (red) samples, accordingly.

scanning electron microscope. The catalyst extrudate samples were placed on aluminum SEM stubs using conductive carbon tape. The SEM images were recorded using secondary electrons (2–10 kV, 0.1 nA). Elemental mapping was performed using a silicon drift detector (SDD) X-MAX from Oxford Instruments. FIB-SEM images were recorded similarly as described in the literature.¹⁸ In brief, a 3 μm thick protective layer of Pt was deposited on top of the region of interest. Trenches were made perpendicular to the surface using the Ga-ion beam (30 kV, 0.43 nA). After milling, a cleaning step followed before imaging in backscatter mode (2–10 kV, 0.1 nA). The diffusion studies of probe molecules and the chemical imaging of the spent samples are described elsewhere and details on the procedures applied can be found in this reference.¹⁷ In short, chemical imaging was performed using a Nikon A1R CFM instrument equipped with a pin hole to filter out-of-focus light. A Nikon $\times 10/1.14$ PLAN APO air objective was used along with a spectral analyzer in the Nikon A1 system, equipped with 32 photomultiplier tubes (PMTs) set to collect emission light in the region of 487–720 nm (resolution of 10 nm). To ensure that the entire surface of each sample was imaged in focus, 50–100 images were recorded at various stage heights (step size = 1 μm) and were stacked showing the maximum intensity value at each pixel.

Catalytic Testing

The catalytic performance of the samples was tested in an *operando* UV–vis spectroscopy setup for performing MTH reactions. Approximately 69 mg of catalyst materials was placed in a fixed-bed reactor using a weight hourly space velocity (WHSV) of 9 h^{-1} at 350–500 $^{\circ}\text{C}$. Methanol and the reaction products were measured by an Interscience compact gas chromatograph (GC). The set-up is equipped with an AvaSpec 2048L spectrometer via a high-temperature UV–vis optical fiber probe, which enables recording of *operando* UV–vis diffuse reflectance spectroscopy (DRS) data. More details of the experimental set-up can be found elsewhere.^{19,20}

RESULTS AND DISCUSSION

In this study, starches were used as pore-forming agents in zeolite-based shaped catalyst bodies to investigate their effect on the pore architecture and catalytic performance in the MTH reaction. Starches of different sizes were chosen, specifically starches from wheat, corn, and potato. After calcination for removing the starches, the samples were compared with a reference sample in which no porogen was added. SEM images, as shown in Figure 1, revealed the morphology of the different starches. It can be observed from the images displayed in Figure 1a–c that each type of starch

consists of spherical particles of various sizes. The SEM images were used to measure the particle size distribution by counting the diameter of at least 100 particles for each sample. The particle size distribution for wheat (green), corn (blue), and potato (red) starches is shown in Figure 1d–f. For wheat starch (green), the mean particle size is 8.4 μm and the particle size varies from 3.3 to 14.1 μm . Corn starch exhibits a mean particle size of 14.5 μm , ranging from 4.6 to 27.3 μm , while potato starch has a mean particle size equal to 29.2 μm , varying from 12.2 to 62.6 μm . Wheat starch shows the narrowest distribution, while corn and potato starch have broader particle size distribution.

Figure 2a illustrates the XRD patterns of the reference (no porogen) and the three samples where wheat, corn, or potato starch were used as a porogen. In general, XRD shows characteristic peaks of an MFI structure for all samples. Thus, the addition and removal of the porogen did not influence the framework structure of zeolite ZSM-5. From the data obtained from NH_3 -TPD measurements, shown in Figure 2b, the total amount and the strength of the acid sites are determined for the different samples under investigation. All samples show two major TPD peaks representing two categories of acid sites, namely, the weak and the strong sites.^{21–24} The reference samples show one peak at $\sim 236 \text{ }^{\circ}\text{C}$ and one at $\sim 435 \text{ }^{\circ}\text{C}$. It can be noted that the porogen samples show the same pattern. However, upon closer inspection, there is a slight shift toward lower temperatures for the porogen-added samples as the TPD peak, corresponding to the weak acid sites, is shifted to $\sim 232 \text{ }^{\circ}\text{C}$, while the TPD peak, corresponding to the strong acid sites are shifted to $\sim 429 \text{ }^{\circ}\text{C}$. The latter implies a weakening of the acid sites, which can be attributed to the decomposition of starch during calcination. According to literature, starches are decomposed around ~ 300 – $350 \text{ }^{\circ}\text{C}$, while water (H_2O), carbon dioxide (CO_2), and carbon monoxide (CO), among other gases, are produced.^{25,26} Thus, the water (H_2O) produced in combination with the calcination temperature could justify the deterioration of the acid sites. There is also a small increase in acidity when wheat starch is used, and it is further increased when corn and potato starch are used. It is essential to remember that, in every sample, the zeolite-to-binder ratio and the total amount of zeolite and binder are

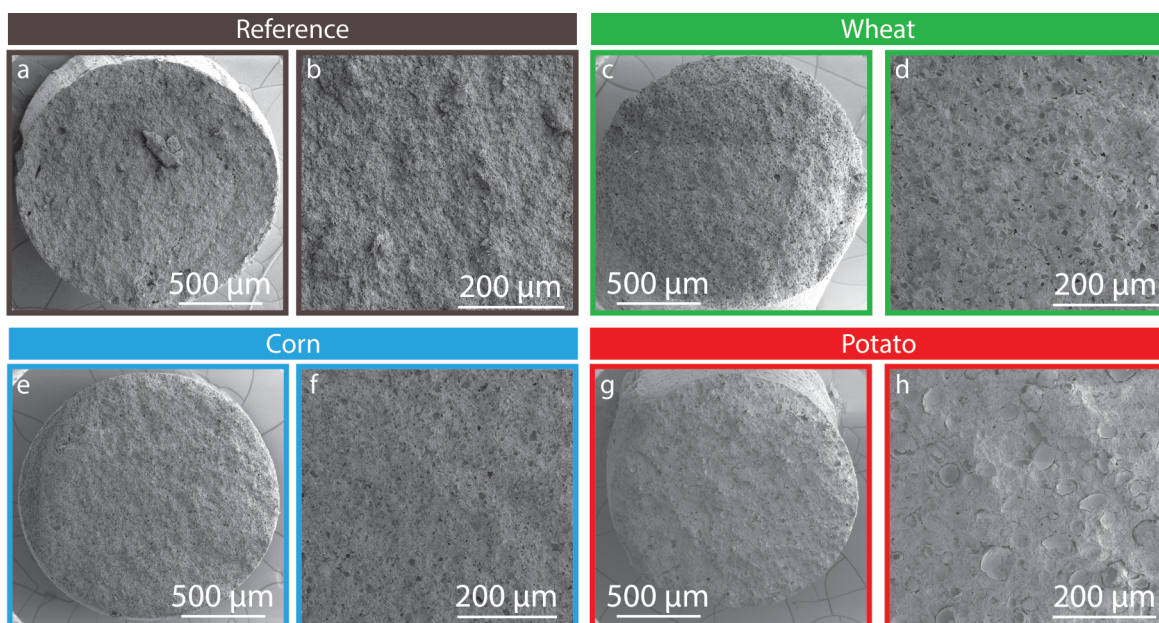


Figure 3. Morphological changes upon pore-forming agent addition. (a, c, e, and g) Low magnification SEM image of the reference sample and the wheat (green), corn (blue), and potato (red) samples, and (b, d, f, and h) corresponding higher magnification SEM images.

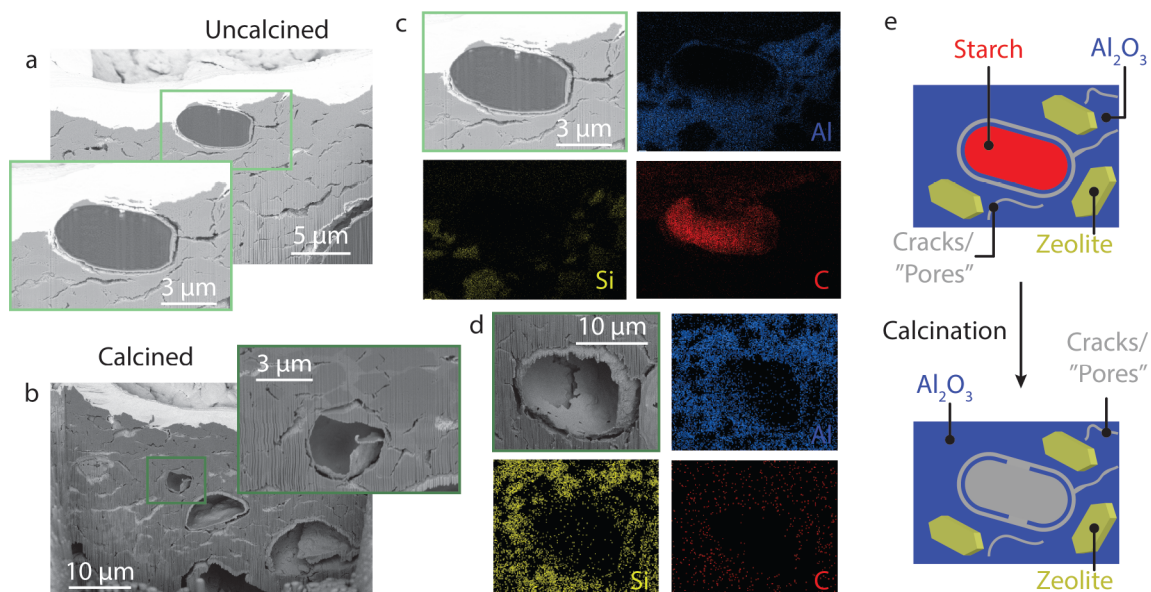


Figure 4. Unravelling the formation of the “broken eggshells”. (a, b) FIB-SEM cross-sectional image of noncalcined and calcined wheat sample; (c, d) EDX analysis and elemental maps for Al (blue), Si (yellow), and C (red) of noncalcined and calcined wheat sample; (e) schematic representation of pore architecture before and after calcination.

constant. Thus, this cannot explain the observed increase of the number of acid sites. It is known that the dispersion of the binder material in combination with mechanical mixing during the extrusion process results in close contact between binder and zeolite, which can lead to the coverage and blockage of the micropores of the zeolite. However, the addition of porogens and the subsequent increase in porosity could explain the rise in acidity as the extra pores formed would facilitate the diffusion of NH_3 into the zeolite pores.

The collected SEM data, as shown in Figure 3, illustrate the morphology of shaped catalyst bodies. The surface of the reference sample shows a compact structure, and some large macropores are present. Moving to the samples in which

porogens were used and after their removal, the higher magnification SEM image (e.g., Figure 3d, f, h) shows the presence of large macropores of different sizes. It is evident that the porogens, after removal, had a significant impact on the porosity of the samples as large macropores were created.

The macropores have the shape of “broken eggshells”, which is more evident for the sample where potato starch was used.

To further understand the formation of the “broken eggshell”, focused ion beam-scanning electron microscopy coupled with electron-dispersive X-ray analysis (FIB-SEM-EDX) was employed before and after the removal of the porogen. SEM images are collected using back-scattered electrons (BSE), and thus, the difference in the contrast

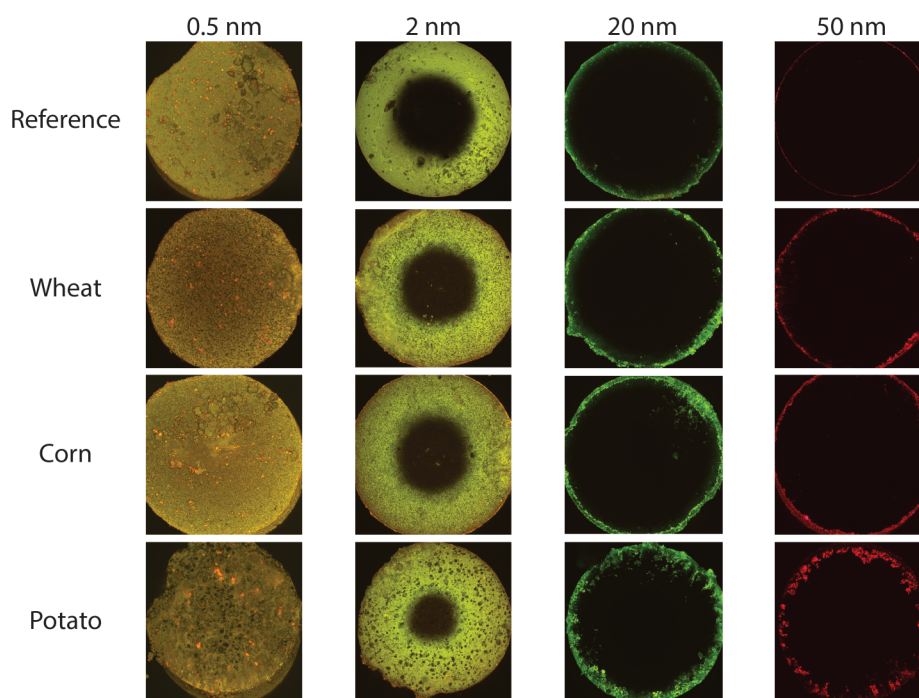


Figure 5. Visualizing accessibility in zeolite-based shaped catalyst bodies. 24 h incubation time with fluorescent nanoprobe of different sizes (0.5, 2, 20, and 50 nm) in shaped zeolite-containing catalyst bodies as measured with CFM.

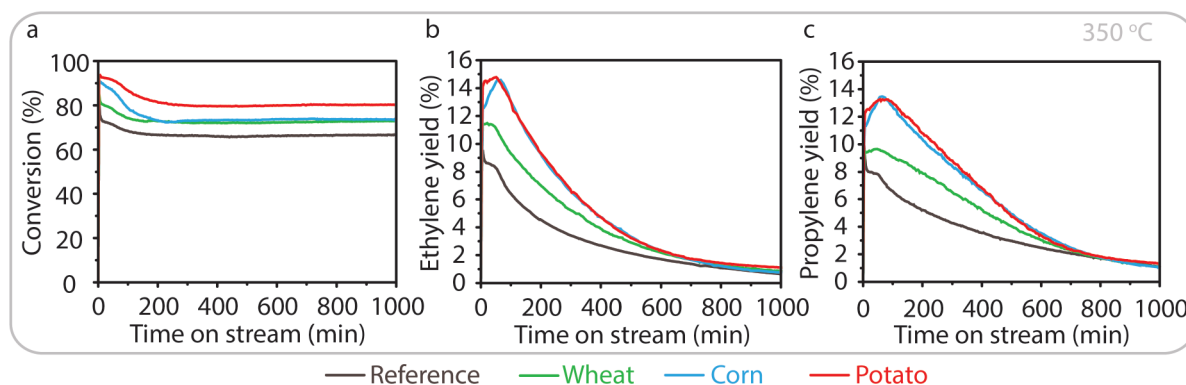


Figure 6. Catalytic behavior in the MTH reaction. Catalytic activity and selectivity of the reference (brown), wheat (green), corn (blue), and potato (red) samples versus TOS (min) for the MTH reaction at 350 °C. (a) Methanol conversion, (b) ethylene, and (c) propylene yield.

depends on the element's atomic number (Z). Therefore, the organic porogen particle and the inorganic part of the material would have different BSE intensities. As a result, the oval dark gray particle in Figure 4a is attributed to the porogen, while the rest of the light gray material is a mixture of zeolite and binder. The white color on top of the surface is the protective layer of Pt to avoid artifacts. Figure 4a shows the FIB-assisted cross-section of the noncalcined wheat sample. It can be seen that the porogen particle is encapsulated in a thin layer of binder material that is further surrounded by free space. EDX maps confirm that the dark gray particle is the organic wheat starch particle enclosed in the alumina binder. After calcination, as displayed in Figure 4b, the inside morphology is similar to that before calcination. The only difference is that removing the porogen has left big spherical pores where the porogen particles were. The thin binder layer, which encapsulated the porogen particles, seems to maintain its shape, but in some cases, this “capsule” is broken, justifying the presence of “broken eggshells”. EDX maps, as shown in Figure 4d, confirm

the observations mentioned above as it is clear that the remaining “shell” consists of alumina binder. There is no trace of carbon species, proving the effective removal of the pore-forming agent. The observations mentioned above are presented schematically in Figure 4e.

To determine the changes in molecular diffusion and pore architecture due to the use of porogens of different sizes, 24 h incubation time studies with fluorescent nanoprobe in the samples under study were performed with CFM. A similar approach has been previously used by our research group to study the pore architecture of zeolite-based shaped catalyst bodies.¹⁷ Four fluorescent probes with different sizes were chosen, namely, those with a size of 0.5 nm (i.e., resorufin), 2 nm (i.e., perylene diimide, PDI), 20 nm (fluospheres), and 50 nm (fluospheres). As illustrated in Figure 5, the smallest nanoprobe thoroughly penetrates the whole extrudate after 24 h incubation time in every sample. As expected, in the reference sample, there is a decrease in penetration depth by increasing the size of the nanoprobe. When incubated with a

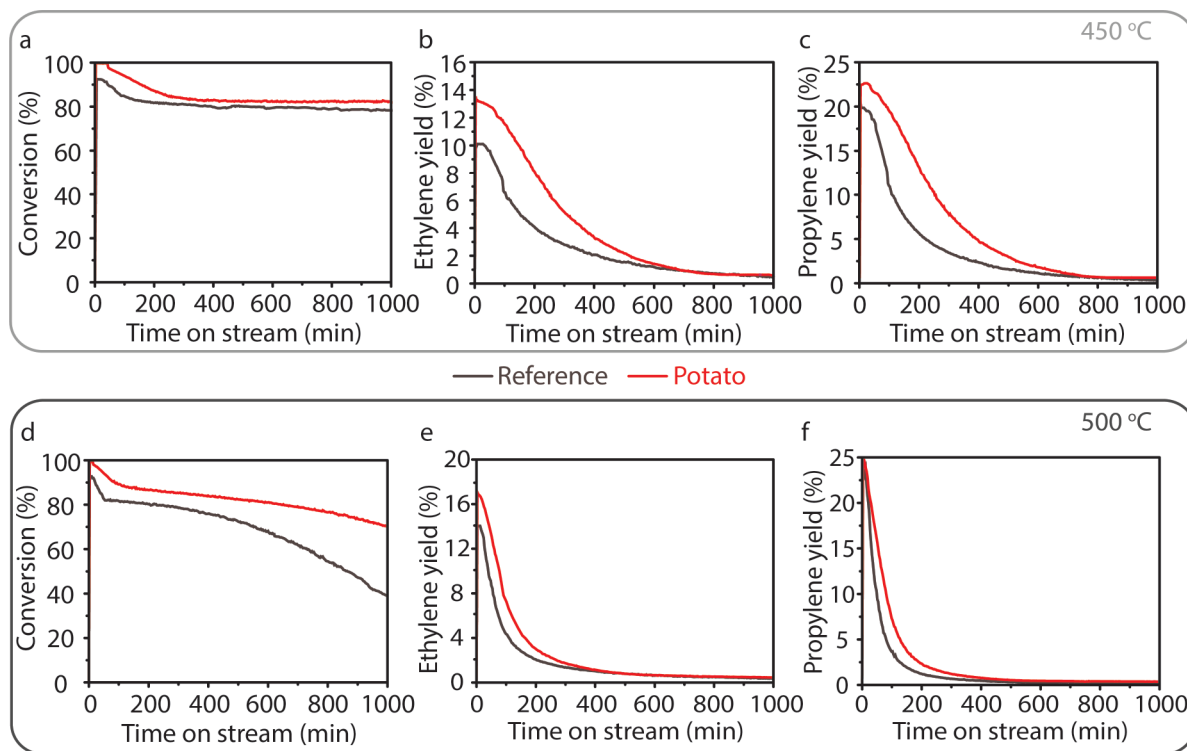


Figure 7. Pore-forming agents versus reaction temperature. Catalytic activity and selectivity of the reference (brown) and potato (red) samples versus TOS for the MTH reaction at 450 °C and 500 °C. (a) Methanol conversion, (b) ethylene, and (c) propylene yield at 450 °C and (d) methanol conversion, (e) ethylene, and (f) propylene yield at 500 °C.

20 nm probe, a thin layer exists, showing a minimal penetration, while the 50 nm hardly shows any penetration. Upon adding pore-forming agents, the 2 nm probe shows a slightly higher penetration for the wheat and corn starch and even higher uptake for the potato starch. Regarding larger fluorescent probes, such as the 20 nm probe, it is clear that the addition of porogens facilitates the diffusion due to the formation of large pores.

For the 50 nm probe, it was found that there is only slight penetration for the wheat and corn samples, while the potato sample shows some fluorescent nanoprobe penetration. However, the potato sample does not present a uniform front of penetration, which implies that the larger pores formed, allowing the diffusion of such large fluorescent probe (50 nm), are not interconnected. Overall, the latter proves the effect of porogens in the shaped zeolite-based catalyst bodies as they increase the porosity and facilitate molecular diffusion. Furthermore, it is noted that the particle size of the porogen could influence the level of porosity and accessibility. Similar observations have been made by our research group when studying catalyst extrudates with different porous binders.¹⁷ It was found that higher uptake profiles of fluorescent nanoprobe could be achieved using highly porous media.

In a next step of our study, we have evaluated the catalytic conversion of methanol and the yields toward ethylene and propylene formed during the Methanol-to-Hydrocarbons (MTH) reaction at 350 °C for the reference extrudate sample, as well as for the samples in which porogens were used. The results are summarized in Figure 6. Initially, the reference sample exhibits high methanol conversion (~81%), while the samples in which pore-forming agents were used show higher conversion, namely, ~85%, ~90%, and ~93% for the wheat, corn, and potato samples, respectively. All samples follow an

induction period after ~250 min time-on-stream (TOS), and the methanol conversions are stabilized at ~66%, ~72%, ~72%, and ~80% for the reference, wheat, corn, and potato sample, respectively. Considering that the MTH reaction is an acid-catalyzed reaction,^{4,27–32} the latter findings are in line with the NH_3 -TPD results as it was shown that the use of porogens increased the overall acidity of the samples under study. Furthermore, the increase in the size of the porogen also affected the degree of accessibility, as previously proven by nanoprobe diffusion studies and consequently the conversion. The same trends are observed for the yields toward light olefins, such as ethylene and propylene. For example, at ~60 min TOS, it can be noted that the reference sample exhibited ~8.2% and ~7.5% yield of ethylene and propylene, while the wheat sample showed ~11% and ~9.5% and the corn and the potato were comparable and exhibited ~14.5% and ~13.1%, respectively. It is worth mentioning that the addition of wheat starch as a pore-forming agent results in a 34% and 27% increase in the absolute yield of ethylene and propylene, respectively, while in the case of corn and potato starch, this increased further to 77% and 74% for ethylene and propylene, respectively. Thus, adding a pore-forming agent increases the accessibility and the diffusion of molecules in and out of the zeolite pores where the active acid sites are located. Furthermore, the ethylene-to-propylene ratio is constant and independent of the addition of the porogen and the size of the starch used. It is also observed that even though the catalytic conversion stays at high levels for at least 1000 min TOS, the formation of ethylene and propylene declines, implying the deactivation due to the pore blockage of the zeolite pores.^{19,33–36}

The effect of the reaction temperature was studied in parallel with the impact of pore-forming agents, as illustrated in Figure

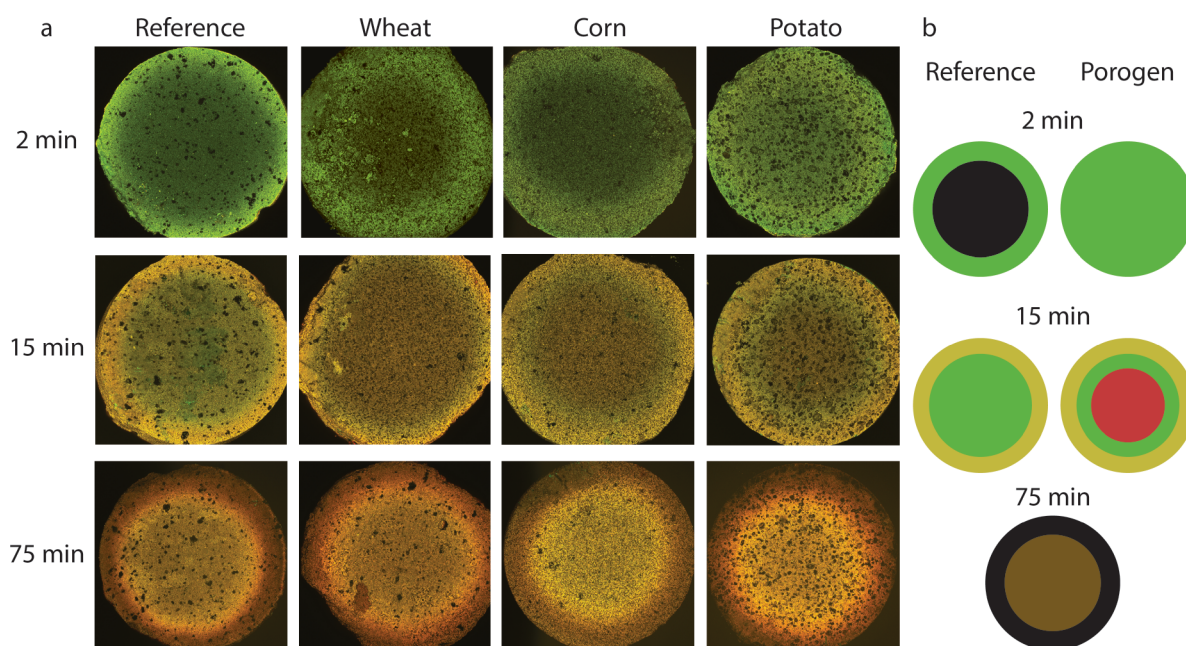


Figure 8. Visualizing the early stages of deactivation in zeolite-based shaped catalyst bodies. (a) Top-view of 3D CFM images of bisected spent extrudates in the MTH reaction at 350 °C after 2, 15, and 75 min TOS. (b) Schematic representation of the significant top-view patterns of reference versus porogens.

7. Thus, the reactions were repeated at 450 and 500 °C for the reference and the sample in which potato starch was used, as it was the one that performed best at 350 °C. Firstly, increasing the reaction temperature to 450 °C resulted in an increase in the conversion as the reference sample exhibits ~92% and the potato sample reaches complete conversion while they exhibited ~81% and ~93%, respectively, at 350 °C. The same level of conversion is noted at 500 °C for both samples. These results align with previous studies on zeolite ZSM-5 in which an overall increase in the formation of light olefins and, especially, preferential formation of propylene than ethylene is reported.^{37–39} We can also notice at higher temperatures that even if we achieve high conversion values, the formation of ethylene and propylene declines faster. For example, at 450 °C, yields toward light olefins decreased drastically after ~100 and ~300 min TOS for the reference and potato samples, accordingly. Similar trends are noted at 500 °C as there is only minor ethylene and propylene production after ~100 min TOS, implying the fast deactivation occurring at higher temperatures. Comparing the two samples, the samples in which potato was used showed the higher formation of light olefins. Furthermore, it is essential to mention that there is a distinct difference when potato starch is used as porogen, as the catalyst exhibits a longer lifetime because there is the formation of light olefins for a longer TOS. Thus, the usage of a porogen increases the catalyst's lifetime even when tested under harsh reaction conditions and higher reaction temperatures when suffering from intense and fast coke rate formation.

In a next stage of our study, CFM was performed on the spent samples after 2, 15, and 75 min TOS to elucidate the effect of the porogens on the catalyst extrudates. During the MTH reaction, a variety of products can be formed such as alkylated benzenes, naphthalene, alkylated phenanthracenes, pyrenes, and larger polyaromatic species. These products can be separated into “less conjugated” and “more conjugated”

species. The first category of molecules, which we coin “less conjugated”, consists of alkylated benzenes and naphthalene, and the last category of molecules, which we coin “more conjugated”, consists of alkylated phenanthracenes, pyrenes, and larger polyaromatic compounds. Two lasers, 488 and 642 nm, were used simultaneously to ensure the maximum excitation of these two categories of hydrocarbons formed during the MTH process. The analytical approach resulted in the emission of green fluorescence from the “less conjugated” species and red fluorescent from the “more conjugated” species.

The top-view 3D CFM images of the reference sample at 2–75 min TOS are presented in Figure 8. After 2 min TOS, a green fluorescent near-edge region exists, while the core appears to be a nonfluorescent region. The phenomenon mentioned above is a first indication of the existence of a transport boundary, which has also been reported before in the literature, and is also visible from the 2 nm nanoprobe diffusion studies in Figure 5. After 15 min TOS, we observe the apparent existence of two regions as there is a yellow near-edge region and a green core region. The yellow near-edge region implies the coexistence of molecules of both categories of molecules, “less conjugated” and “more conjugated”, suggesting the oligomerization of smaller molecules to form larger hydrocarbon species at the near-edge region of the catalyst extrudates and a remaining core of small hydrocarbon molecules. After 75 min TOS, it is evident that the catalyst has already started to deactivate as the near-edge region contains nonfluorescent graphitic coke, which explains the black color, while the core region of the catalyst extrudate has a yellow-orange color. The latter can be explained by the existence of an inaccessible molecular transport boundary caused by non-interconnected pores and pore narrowing as the small molecules are trapped and further oligomerized to larger molecules. The results, as mentioned earlier, are in line with the results presented by our research group. Whiting *et al.*

reported the existence of a molecular transport boundary as well as two distinct fluorescent regions in a similar catalytic system used in the same catalytic reaction.¹⁷ Furthermore, Luna-Murillo *et al.* used the same approach to investigate the formation and the distribution of carbon deposits during the catalytic fast pyrolysis of biomass. Both regions containing “less and/or more conjugated” species and a region of non-fluorescent graphite-like carbon deposits were shown.⁴⁰

Interestingly, in the early stages of the reaction (2 and 15 min TOS), the spent catalyst extrudates in which a porogen was used differ from the reference sample. After 2 min TOS, it can be seen that the wheat and corn samples have a thicker near-edge region of the same color and a nonfluorescent core region with a smaller diameter. For the potato sample, we can observe a uniform formation of species across the cross section due to the increased molecular diffusion in and out of the catalyst extrudate. After 15 min TOS, all three samples appear to have a yellow near-edge region, a red fluorescent core region, and an in-between region with green color. A schematic representation is shown in Figure 8b in order to enable a better visualization of the coke formation pattern of the reference samples versus the porogen-containing samples. The red core region is in stark contrast to that observed in the reference sample. The latter can be explained by the acidity increase upon the addition of porogens (Figure 2). Consequently, this can lead to an increased formation of “less conjugated” species that cannot pass through the molecular transport boundary or diffuse out of the catalyst extrudate. As a result, these molecules will oligomerize to form larger hydrocarbon species (visualized as red fluorescent species). It can also be seen that, with increasing the particle size of the porogens and thereby increasing the degree of accessibility, the red core region becomes smaller. The latter confirms our assumption that even though the acidity is higher in potato starch, the accessibility is also higher. Thus, even though the smaller molecules’ formation is higher, the red core region is smaller as the molecules can diffuse out of the catalyst extrudate, and they do not oligomerize further to form larger hydrocarbon molecules.

CONCLUSIONS

This study reports on the beneficial effect of adding pore-forming agents in shaped zeolite-containing catalyst bodies and the impact of the size of the porogen. Starches from wheat, corn, and potato were used as differently sized porogens, with potato starch having the largest particles. FIB-SEM revealed that starch particles are encapsulated in a shell of binder material, which collapses, forming “broken eggshells” and very large macropores upon calcination. Diffusion studies of nanoprobe of different sizes showed higher penetration depths when potato starch was used. Catalytic testing in the MTH reaction at 350 °C showed that porogen-addition resulted in up to ~12% higher conversion, while there was a 74% and 77% increase in propylene and ethylene yield, respectively. The addition of the porogens also increased the lifetime of the catalyst extrudate, even at higher reaction temperatures. The nature and the location of the species formed during the MTH reaction were studied, and the subsequent changes upon modification in pore architecture due to induced macroporosity. More importantly, this study represents a clear and direct visualization linking pore architecture with molecular transport and catalytic performance in zeolite-based catalyst bodies. Overall, this chemical imaging approach combined with the results from catalytic

performance allows us to understand and design a better MTH catalyst as well as apply this knowledge to other zeolite-based catalyst materials.

AUTHOR INFORMATION

Corresponding Authors

Gareth Whiting – *Inorganic Chemistry and Catalysis group, Debye Institute for Nanomaterials Science & Institute for Sustainable and Circular Chemistry, Utrecht University, 3584 CG Utrecht, The Netherlands; Email: gwhiting1@gmail.com*

Bert M. Weckhuysen – *Inorganic Chemistry and Catalysis group, Debye Institute for Nanomaterials Science & Institute for Sustainable and Circular Chemistry, Utrecht University, 3584 CG Utrecht, The Netherlands; orcid.org/0000-0001-5245-1426; Email: b.m.weckhuysen@uu.nl*

Authors

Nikolaos Nikolopoulos – *Inorganic Chemistry and Catalysis group, Debye Institute for Nanomaterials Science & Institute for Sustainable and Circular Chemistry, Utrecht University, 3584 CG Utrecht, The Netherlands; orcid.org/0000-0002-3722-4388*

Luke A. Parker – *Inorganic Chemistry and Catalysis group, Debye Institute for Nanomaterials Science & Institute for Sustainable and Circular Chemistry, Utrecht University, 3584 CG Utrecht, The Netherlands; Present Address: TNO Environmental Modelling, Sensing and Analysis, Princetonlaa 6, 3584 CB Utrecht, The Netherlands; orcid.org/0000-0002-6041-565X*

Abhijit Wickramasinghe – *Inorganic Chemistry and Catalysis group, Debye Institute for Nanomaterials Science & Institute for Sustainable and Circular Chemistry, Utrecht University, 3584 CG Utrecht, The Netherlands*

Oscar van Veenhuizen – *Inorganic Chemistry and Catalysis group, Debye Institute for Nanomaterials Science & Institute for Sustainable and Circular Chemistry, Utrecht University, 3584 CG Utrecht, The Netherlands*

Complete contact information is available at:
<https://pubs.acs.org/10.1021/cbmi.2c00009>

Notes

The authors declare no competing financial interest.

ACKNOWLEDGMENTS

This research has received funding from the European Union’s EU Framework Program for Research and Innovation Horizon 2020 under Grant Agreement No. 721385 (MSCA-ETN SOCRATES, <https://etn-socrates.eu/>) and the US Army Research Office.

REFERENCES

- (1) Corma, A. Inorganic Solid Acids and Their Use in Acid-Catalyzed Hydrocarbon Reactions. *Chem. Rev.* **1995**, *95*, 559–614.
- (2) Corma, A.; Diaz-Cabañas, M. J.; Martínez-Triguero, J.; Rey, F.; Rius, J. A Large-Cavity Zeolite with Wide Pore Windows and Potential as an Oil Refining Catalyst. *Nature* **2002**, *418*, 514–517.
- (3) Climent, M. J.; Corma, A.; Iborra, S. Heterogeneous Catalysts for the One-Pot Synthesis of Chemicals and Fine Chemicals. *Chem. Rev.* **2011**, *111*, 1072–1133.
- (4) Yarulina, I.; Chowdhury, A. D.; Meirer, F.; Weckhuysen, B. M.; Gascon, J. Recent Trends and Fundamental Insights in the Methanol-to-Hydrocarbons Process. *Nat. Catal.* **2018**, *1*, 398–411.

- (5) Vogt, E. T. C.; Whiting, G. T.; Dutta Chowdhury, A.; Weckhuysen, B. M. Zeolites and Zeotypes for Oil and Gas Conversion. *Adv. Catal.* **2015**, *58*, 143–314.
- (6) Olsbye, U.; Svelle, S.; Lillerud, K. P.; Wei, Z.; Chen, Y.; Li, J.; Wang, J.; Fan, W. The Formation and Degradation of Active Species during Methanol Conversion over Protonated Zeotype Catalysts. *Chem. Soc. Rev.* **2015**, *44*, 7155–7176.
- (7) Chowdhury, A. D.; Houben, K.; Whiting, G. T.; Chung, S. H.; Baldus, M.; Weckhuysen, B. M. Electrophilic Aromatic Substitution over Zeolites Generates Wheland-Type Reaction Intermediates. *Nat. Catal.* **2018**, *1*, 23–31.
- (8) Yilmaz, B.; Müller, U. Catalytic Applications of Zeolites in Chemical Industry. *Top. Catal.* **2009**, *52*, 888–895.
- (9) Chen, N. Y.; Garwood, W. E. Industrial Application of Shape-Selective Catalysis. *Catal. Rev.* **1986**, *28*, 185–264.
- (10) Tanabe, K.; Hölderich, W. F. Industrial Application of Solid Acid-Base Catalysts. *Appl. Catal. A Gen.* **1999**, *181*, 399–434.
- (11) Young, L. B.; Butter, S. A.; Kaeding, W. W. Shape Selective Reactions with Zeolite Catalysts. III. Selectivity in Xylene Isomerization, Toluene-Methanol Alkylation, and Toluene Disproportionation over ZSM-5 Zeolite Catalysts. *J. Catal.* **1982**, *76*, 418–432.
- (12) Yang, K.; Zhang, D.; Zou, M.; Yu, L.; Huang, S. The Known and Overlooked Sides of Zeolite-Extrudate Catalysts. *ChemCatChem* **2021**, *13*, 1414–1423.
- (13) Ertl, G.; Knözinger, H.; Schütch, F.; Weitkamp, J., Eds. *Handbook of Heterogeneous Catalysis*; Wiley-VCH Verlag: Weinheim, 2008.
- (14) Mitchell, S.; Michels, N. L.; Pérez-Ramírez, J. From Powder to Technical Body: The Undervalued Science of Catalyst Scale Up. *Chem. Soc. Rev.* **2013**, *42*, 6094–6112.
- (15) Øygarden, A. H.; Perez-Ramirez, J.; Waller, D.; Schoffel, K.; Brackenbury, D. M. Method for Producing Supported Oxide Catalysts. WO 2004110622A1 Application, 2004.
- (16) Whiting, G. T.; Chung, S. H.; Stosic, D.; Chowdhury, A. D.; Van Der Wal, L. I.; Fu, D.; Zecevic, J.; Travert, A.; Houben, K.; Baldus, M.; Weckhuysen, B. M. Multiscale Mechanistic Insights of Shaped Catalyst Body Formulations and Their Impact on Catalytic Properties. *ACS Catal.* **2019**, *9*, 4792–4803.
- (17) Whiting, G. T.; Nikolopoulos, N.; Nikolopoulos, I.; Chowdhury, A. D.; Weckhuysen, B. M. Visualizing Pore Architecture and Molecular Transport Boundaries in Catalyst Bodies with Fluorescent Nanoprobes. *Nat. Chem.* **2019**, *11*, 23–31.
- (18) De Winter, D. A. M.; Meirer, F.; Weckhuysen, B. M. FIB-SEM Tomography Probes the Mesoscale Pore Space of an Individual Catalytic Cracking Particle. *ACS Catal.* **2016**, *6*, 3158–3167.
- (19) Goetze, J.; Weckhuysen, B. M. Spatiotemporal Coke Formation over Zeolite ZSM-5 during the Methanol-to-Olefins Process as Studied with Operando UV-Vis Spectroscopy: A Comparison between H-ZSM-5 and Mg-ZSM-5. *Catal. Sci. Technol.* **2018**, *8*, 1632–1644.
- (20) Goetze, J.; Meirer, F.; Yarulina, I.; Gascon, J.; Kapteijn, F.; Ruiz-Martínez, J.; Weckhuysen, B. M. Insights into the Activity and Deactivation of the Methanol-to-Olefins Process over Different Small-Pore Zeolites As Studied with Operando UV-Vis Spectroscopy. *ACS Catal.* **2017**, *7*, 4033–4046.
- (21) Uslamin, E. A.; Luna-Murillo, B.; Kosinov, N.; Bruijninx, P. C. A.; Pidko, E. A.; Weckhuysen, B. M.; Hensen, E. J. M. Gallium-Promoted HZSM-5 Zeolites as Efficient Catalysts for the Aromatization of Biomass-Derived Furans. *Chem. Eng. Sci.* **2019**, *198*, 305–316.
- (22) Wang, Y.; Chang, Y.; Liu, M.; Zhang, A.; Guo, X. A Facile Strategy to Prepare Shaped ZSM-5 Catalysts with Enhanced Para-Xylene Selectivity and Stability for Toluene Methylation: The Effect of In Situ Modification by Attapulgite. *Molecules* **2019**, *24*, 3462.
- (23) Whiting, G. T.; Chowdhury, A. D.; Oord, R.; Paalanen, P.; Weckhuysen, B. M. The Curious Case of Zeolite-Clay/Binder Interactions and Their Consequences for Catalyst Preparation. *Faraday Discuss.* **2016**, *188*, 369–386.
- (24) Nikolopoulos, N.; Geitenbeek, R. G.; Whiting, G. T.; Weckhuysen, B. M. Unravelling the Effect of Impurities on the Methanol-to-Olefins Process in Waste-Derived Zeolites ZSM-5. *J. Catal.* **2021**, *396*, 136–147.
- (25) Liu, X.; Khor, S.; Petinakis, E.; Yu, L.; Simon, G.; Dean, K.; Bateman, S. Effects of Hydrophilic Fillers on the Thermal Degradation of Poly(Lactic Acid). *Thermochim. Acta* **2010**, *509*, 147–151.
- (26) Beda, A.; Yamada, H.; Egunov, A.; Ghimbeu, C. M.; Malval, J. P.; Saito, Y.; Luchnikov, V. Carbon Microtubes Derived from Self-Rolled Chitosan Acetate Films and Graphitized by Joule Heating. *J. Mater. Sci.* **2019**, *54*, 11345–11356.
- (27) Stöcker, M. Methanol-to-Hydrocarbons: Catalytic Materials and Their Behavior. *Microporous Mesoporous Mater.* **1999**, *29*, 3–48.
- (28) Haw, J. F.; Song, W.; Marcus, D. M.; Nicholas, J. B. The Mechanism of Methanol to Hydrocarbon Catalysis. *Acc. Chem. Res.* **2003**, *36*, 317–326.
- (29) Yarulina, I.; Bailleul, S.; Pustovarenko, A.; Martínez, J. R.; Wispelaere, K. D.; Hajek, J.; Weckhuysen, B. M.; Houben, K.; Baldus, M.; Van Speybroeck, V.; Kapteijn, F.; Gascon, J. Suppression of the Aromatic Cycle in Methanol-to-Olefins Reaction over ZSM-5 by Post-Synthetic Modification Using Calcium. *ChemCatChem* **2016**, *8*, 3057–3063.
- (30) Rostamizadeh, M.; Yaripour, F. Dealumination of High Silica H-ZSM-5 as Long-Lived Nanocatalyst for Methanol to Olefin Conversion. *J. Taiwan Inst. Chem. Eng.* **2017**, *71*, 454–463.
- (31) Chowdhury, A. D.; Houben, K.; Whiting, G. T.; Mokhtar, M.; Asiri, A. M.; Al-Thabaiti, S. A.; Basahel, S. N.; Baldus, M.; Weckhuysen, B. M. Initial Carbon–Carbon Bond Formation during the Early Stages of the Methanol-to-Olefin Process Proven by Zeolite-Trapped Acetate and Methyl Acetate. *Angew. Chem. Int. Ed.* **2016**, *55*, 15840–15845.
- (32) Tian, P.; Wei, Y.; Ye, M.; Liu, Z. Methanol to Olefins (MTO): From Fundamentals to Commercialization. *ACS Catal.* **2015**, *5*, 1922–1938.
- (33) Mores, D.; Stavitski, E.; Kox, M. H. F.; Kornatowski, J.; Olsbye, U.; Weckhuysen, B. M. Space- and Time-Resolved In-Situ Spectroscopy on the Coke Formation in Molecular Sieves: Methanol-to-Olefin Conversion over H-ZSM-5 and H-SAPO-34. *Chem.—Eur. J.* **2008**, *14*, 11320–11327.
- (34) Mores, D.; Kornatowski, J.; Olsbye, U.; Weckhuysen, B. M. Coke Formation during the Methanol-to-Olefin Conversion: In Situ Microspectroscopy on Individual H-ZSM-5 Crystals with Different Brønsted Acidity. *Chem.—Eur. J.* **2011**, *17*, 2874–2884.
- (35) Nordvang, E. C.; Borodina, E.; Ruiz-Martínez, J.; Fehrmann, R.; Weckhuysen, B. M. Effects of Coke Deposits on the Catalytic Performance of Large Zeolite H-ZSM-5 Crystals during Alcohol-to-Hydrocarbon Reactions as Investigated by a Combination of Optical Spectroscopy and Microscopy. *Chem.—Eur. J.* **2015**, *21*, 17324–17335.
- (36) Rownaghi, A. A.; Rezaei, F.; Hedlund, J. Uniform Mesoporous ZSM-5 Single Crystals Catalyst with High Resistance to Coke Formation for Methanol Deoxygenation. *Microporous Mesoporous Mater.* **2012**, *151*, 26–33.
- (37) Ivanovna, K. R.; Yurievich, P. A. Effect of Temperature on Ethanol Conversion over the Surface of Zr-Modified Zeolite ZSM-5. *Catal. Sustain. Energy* **2016**, *2*, 83–86.
- (38) Ilias, S.; Khare, R.; Malek, A.; Bhan, A. A Descriptor for the Relative Propagation of the Aromatic- and Olefin-Based Cycles in Methanol-to-Hydrocarbons Conversion on H-ZSM-5. *J. Catal.* **2013**, *303*, 135–140.
- (39) Dehertog, W. J. H.; Froment, G. F. Production of Light Alkenes from Methanol on ZSM-5 Catalysts. *Appl. Catal.* **1991**, *71*, 153–165.
- (40) Luna-Murillo, B.; Pala, M.; Paioni, A. L.; Baldus, M.; Ronsse, F.; Prins, W.; Bruijninx, P. C. A.; Weckhuysen, B. M. Catalytic Fast Pyrolysis of Biomass: Catalyst Characterization Reveals the Feed-Dependent Deactivation of a Technical ZSM-5-Based Catalyst. *ACS Sustain. Chem. Eng.* **2021**, *9*, 291–304.